Secondary Frequency Support to Weak Grids through Coordinating Control of Hybrid HVDC System

Jagdeep Kaur, *Student Member, IEEE*, and Nilanjan Ray Chaudhuri, *Senior Member, IEEE*

***Abstract*—A recently proposed Hybrid-High Voltage DC (HVDC) system comprising a Capacitor Commutated Converter connected in series with a 2-stage Voltage Source Converter called 'Vernier' on the DC side and in parallel on the AC side is considered to transfer power from onshore wind farms (WFs) to the load centers. The flexible DC voltage polarity of the Vernier gives rise to circulating power. Although the circulating power leads to unwanted losses, it can be leveraged as an additional degree of freedom. This extra degree of freedom is used to provide secondary frequency control in the inverter-side grid by extracting power from the rectifier without any communication of signals while maintaining constant margin angle and firing angle at the respective ends. Moreover, to improve the rectifier-side grid frequency, the WFs provide primary frequency support while operating under deloaded condition. Analytical insight into this complex system is developed to damp frequency oscillations and increase utilization of Vernier capacity.**

***Index Terms*—CCC, Hybrid HVDC, VSC, weak grid.**

I. Introduction

OFTEN large wind farms (WFs) are connected to smaller and geographically remote portions of the grids, which are weak in nature. The major load centers can be quite far from such WFs needing power transmission over long distances, which can be realized with High Voltage DC (HVDC) technology. Also, it is not uncommon to have low short circuit capacity in the load centers, which reduces the strength of grid on the receiving end. In such conditions the grids on both sides of the HVDC link will be weak in nature.

The focus of this paper is secondary frequency regulation (also called Automatic Generation Control or AGC) of load centers connected to weak grids at the HVDC inverter-end in order to prevent the frequency from falling in the underfrequency load shedding (UFLS) range. Unlike primary frequency control, AGC brings frequency back to its nominal value and requires minutes to do that [1]. As opposed to traditional AGC, the HVDC inverter can be equipped with frequency regulation loops, which can perform the same task quickly. Such frequency controllers have been implemented in Hokkaido-Honshu HVDC link, Nelson River HVDC, Basslink interconnector, and in New Zealand DC link [2]–[6] – all of which are based on Line Commutated Converter (LCC) technology. Unfortunately, LCC-HVDC faces major challenges under weak grid scenario [7]. Although Voltage Source Converter (VSC) HVDC can solve this issue [8] and control frequency at the inverter-side grid [9], [10]; this technology is still not mature compared to LCC considering bulk power transfer, efficiency, and DC-fault protection. To operate under weak grid condition, all of the LCC projects [2]–[6] employed synchronous condensers. However, synchronous condensers are very costly, need additional maintenance, and give rise to unwanted issues like electromechanical oscillations. Such issues were observed in the Nelson River HVDC project [2] and the New Zealand DC link [6]. An alternative to LCC-HVDC is the Capacitor Commutated Converter (CCC) technology [11], which can deal with issues associated with weak AC networks. However, all CCC-HVDC projects so far considered back-to-back connections [12]–[14].

Point-to-point Hybrid-HVDC concepts have also been proposed by researchers in multiple forms, which involve LCCs and Self Commutated Converters (SCCs), e.g. VSCs [15]–[25]. However, there is hardly any tangible research done on CCC or Hybrid HVDC for the secondary frequency control.

In order to take advantage of both CCC and VSC, the hybrid scheme and its coordinating control are proposed and analyzed in references [26], [27]. The Hybrid scheme consists of a CCC connected in series on the DC side and in parallel in the AC side with a 2-stage VSC called the 'Vernier'. The advantages of this Hybrid HVDC system are as follows: (a) significant reduction in the switched capacitors by maintaining net reactive power consumption almost constant over a range of operating conditions; (b) elimination of converter-transformer tap changers both at rectifier and inverter buses by DC voltage regulation through Vernier; (c) enhanced power flow recovery and reduction in commutation failure following severe disturbances. The benefits of this system are explained in detail in reference [27].

In this paper, we explore the possibility of secondary

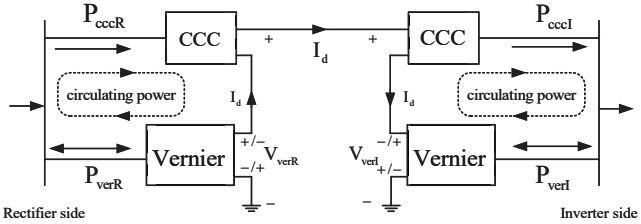

Fig. 1. Block-diagram representation of the point-to-point Hybrid HVDC link highlighting the direction of circulating power.

The authors are with the School of Electrical Engineering and Computer Science, Pennsylvania State University, University Park, PA, USA (e-mail: *juk415@psu.edu, nuc88@psu.edu*).

Financial support from NSF Grant Award ECCS 1656983 is gratefully acknowledged.

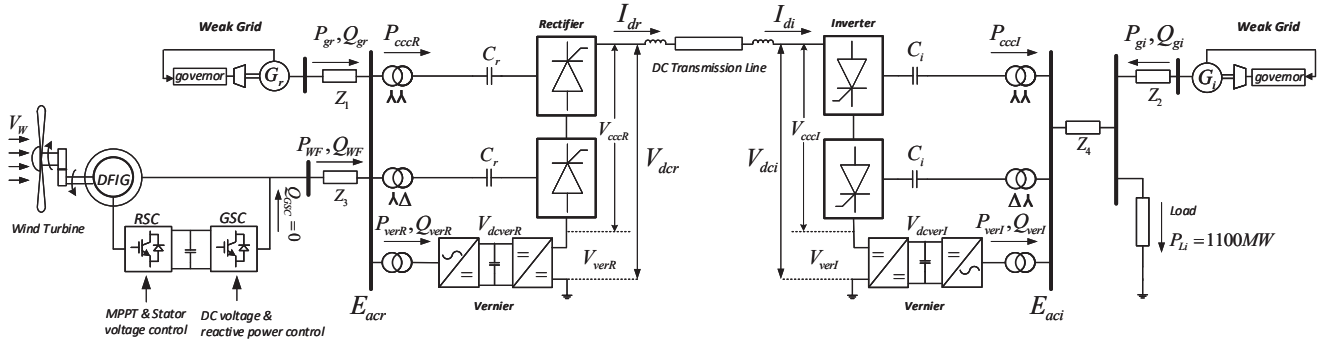

Fig. 2. Hybrid HVDC system connecting WF in rectifier-end and load center in inverter-side. See Appendix for parameters.

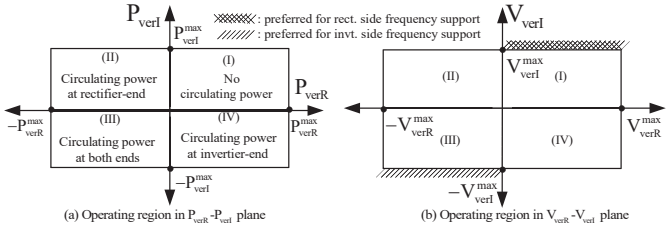

Fig. 3. Operating region of the hybrid HVDC in (a) $P_{verR}-P_{verI}$ plane and (b) $V_{verR}-V_{verI}$ plane. Boundaries preferred for locating nominal operating points before inverter and rectifier frequency support are highlighted.

frequency control using the above-mentioned Hybrid HVDC scheme. The HVDC rectifier side has a weak grid with WFs and its inverter end is connected to a weak grid with load center. The Vernier unit of Hybrid HVDC can alter the magnitude and polarity of its DC output. The flexible voltage polarity of the Vernier leads to circulating power, which gives rise to unwanted losses. However, this circulating power gives additional degrees of freedom to the control scheme, which can be used to regulate the frequency at the inverter-side grid under any disturbance. This is done by extracting power from the rectifier end without any change in the reactive power consumption or any communication of signals. This enables the HVDC link to act as a "conduit" of frequency support, thereby allowing it to earn revenue and compensate for losses due to circulating power. Moreover, deloaded WFs are utilized to provide primary frequency support to the rectifier-side AC grid. Analytical insight into this complex system is developed to damp frequency oscillations and improve utilization of Vernier capacity.

II. Circulating Power in Hybrid-HVDC System for Frequency Support Provision

Figure 1 shows a block-diagram of the point-to-point Hybrid HVDC link to represent the directions of real power flows, DC current, and polarities of DC voltages. Further details of the Hybrid topology can be found in [26], [27], which are not repeated here. Note that the same DC current I_d is flowing through the DC ports of CCCs and Verniers, and it is unidirectional. In each of the rectifier and the inverter ends, the direction of P_{ccc} always remains the same, i.e. P_{cccR} leaves the DC-side of the rectifier and P_{cccI} enters the DC terminals of the inverter. On the contrary, the real power flowing through the Verniers (P_{verR} and P_{verI}) can be bidirectional. This is because V_{verR} and V_{verI} each can flip its polarity as shown in Fig. 1. When the direction of P_{verR} is opposite to that of P_{cccR}, a circulating power flows in the loop marked in Fig. 1. The same applies to the inverter side.

Figure 3(a) shows the operating region of the Hybrid-HVDC in P_{verR}-P_{verI} plane. The region is bounded by Vernier power ratings $P_{verR}^{max} = V_{verR}^{max} I_d^{max}$ and $P_{verI}^{max} = V_{verI}^{max} I_d^{max}$. The positive values indicate that Vernier powers are in the same direction as the corresponding CCC powers. The four quadrants indicate the existence of circulating power in the rectifier and/or the inverter end. Circulating power is normally undesirable as it leads to system losses. Therefore, under normal circumstances, the system should operate in quadrant I. However, circulating power also provides additional degrees of freedom for selectively providing frequency support to either of the rectifier or inverter-side AC grids while maintaining constant firing angle α_r at the rectifier side and constant extinction angle γ_i in the inverter end.

Utilization of Hybrid-HVDC system for AGC can lead to its participation in a frequency regulation market in future, which can help offset the loss due to circulating power and earn additional revenue. In order to provide AGC action through HVDC on the inverter-side AC system following a loss of generation or increase in load, power flowing through HVDC should be increased. This can be achieved by increasing the reference voltage at the inverter end while maintaining constant I_d and γ_i. The magnitude and polarity of the Vernier voltages decide the amount of circulating power present in the system. Figure 3(b) shows the operating region in the $V_{verR} - V_{verI}$ plane. It will be shown in Section IV that the frequency support is provided only by increasing V_{ver} in order to maintain constant I_d. Hence, a portion of the hashed boundary in Fig. 3(b) is preferred for nominal operation of V_{ver}. For frequency support to the rectifier-side AC system following rectifier-side load increase or generation loss, the reference voltage of the inverter control need to be reduced to extract less power from the rectifier end. Again, this is accomplished by solely redcing V_{ver}. Therefore, another portion of the closed boundary in Fig. 3(b) is preferred for nominal operation of V_{ver}. In this paper, we focus on the frequency support to the inverter-side AC grid, which is described next.

III. Secondary Frequency Control on Inverter Side Grid

We consider a Hybrid HVDC system connecting WF in rectifier-end and load center in the inverter-end as shown in Fig. 2. AC grids at both ends are considered weak – see Appendix

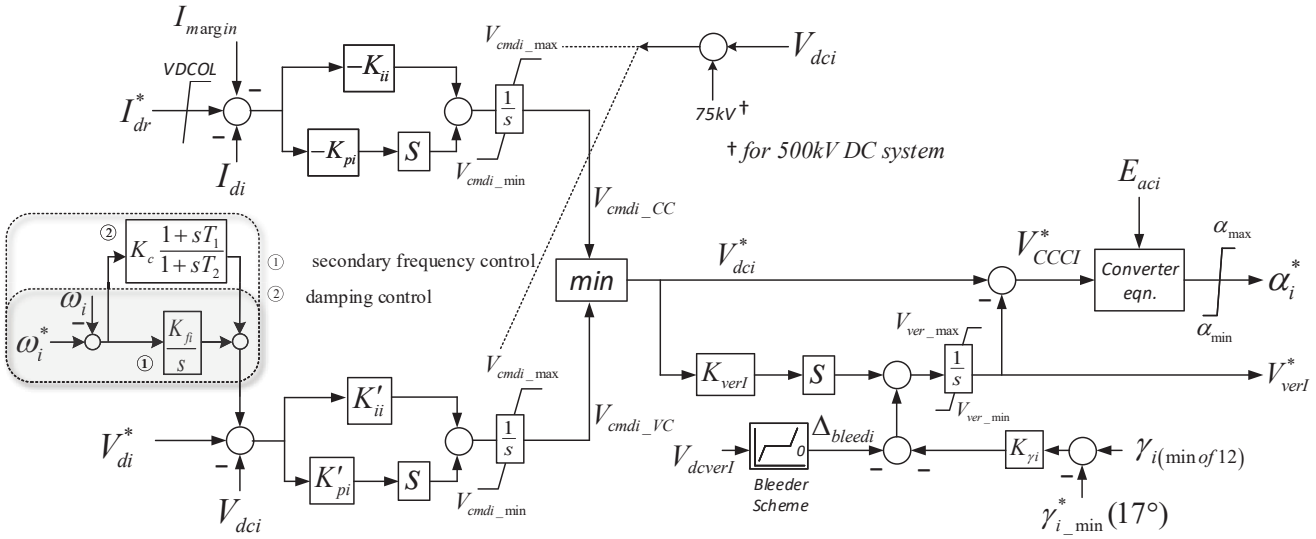

Fig. 4. Proposed modification in inverter coordinating control of Hybrid-HVDC system with secondary frequency regulation and damping control.

for system parameters. To utilize HVDC for AGC action at the inverter-side grid following loss of generation or load increase, the inverter coordinating control in [27] needs to be modified as described next.

A. Proposed Inverter Control

Inverter-side coordinating control aims to keep the total inverter DC voltage and CCC margin angle constant, which was presented in our previous work [27]. A supplementary integral control that drives the inverter-side angular frequency deviation $\Delta\omega_i$ to zero is proposed to modulate the reference DC voltage of the inverter, see dotted box in Fig. 4. A lead-lag compensator is used to improve system damping, which will be discussed later. From Fig. 4, the effect of the addition of a supplementary control on the change in voltage command V^*_{dci} (note that V^*_{dci} is different from V^*_{di}) can be derived as:

$$\Delta V^*_{dci} = \frac{K_{fi}}{s}\left(K'_{pi} + \frac{K'_{ii}}{s}\right)\Delta\omega_i \tag{1}$$

Considering tight control over the margin angle γ_i, the CCC voltage will be affected negligibly with the change in voltage command from equation (1). Therefore, the change in Vernier voltage will be directly affected by the change in V^*_{dci}, which is given by:

$$\Delta V^*_{verI} = K_{verI}\Delta V^*_{dci} \tag{2}$$

Since the rectifier-side control shown in Fig. 5 maintains a constant DC current I_{dr} (and I_{di}) and constant firing angle α_r, the power consumption of the inverter CCC does not change. Therefore, this change in V_{verI} changes the power consumed by the Vernier and thus alters the circulating power. Using this degree of freedom, extra power required to compensate the inverter-side generation loss or increase in load comes from the rectifier end. If this power change in the rectifier-side AC grid comes entirely from the governor droop action of the generating unit G_r shown in Fig. 2, it will result in significant reduction of the rectifier-end frequency. To reduce frequency deviation Δf_r, the DFIG-based WF can be used to provide primary frequency support, which is explained next.

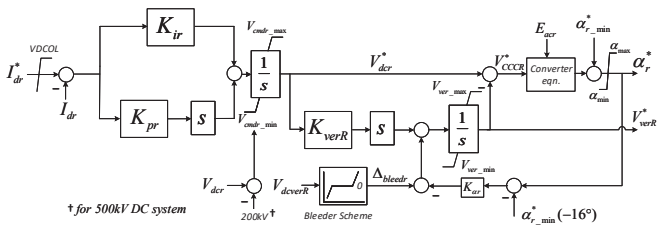

Fig. 5. Rectifier coordinating control of Hybrid-HVDC system [27].

B. Primary Frequency Support from WF

To reduce the frequency deviation of the rectifier-side grid, the DFIG-based WF operates with power-frequency-droop control [28] under deloaded condition. The droop control ensures power sharing between G_r and the WF power reserve under abnormal conditions. The mechanical power input to the wind turbine can be expressed as:

$$P = \omega_r T^* = K_{off}\omega_r^3 + K_{wf}\Delta f_r \tag{3}$$

where, ω_r: rotor speed, T^*: torque reference, $K_{off} = K_d * K_{opt}$, K_d: deloading factor ($= 0.9$), K_{opt}: coefficient used for maximum power point tracking (MPPT), K_{wf}: frequency

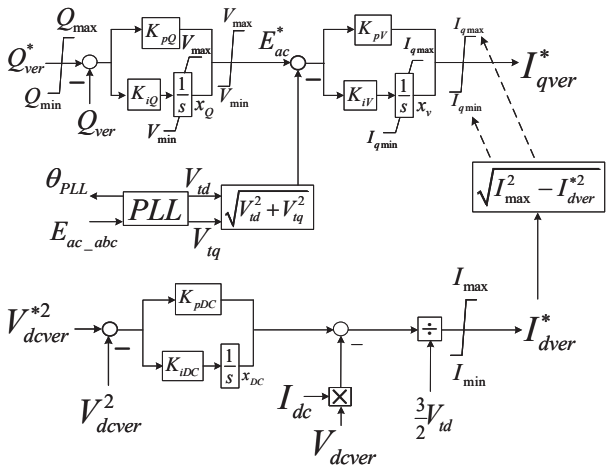

Fig. 6. Vernier AC-DC converter controls (rectifier and inverter-side): Outer reactive power control loop, AC voltage control, DC-link voltage control, and current limiting strategy.

droop coefficient. From equation (3), T^* can be expressed as:

$$T^* = K_{off}\omega_r^2 + \frac{K_{wf}\Delta f_r}{\omega_r} \tag{4}$$

The reference torque is used to generate the reference current component of the RSC control as describe in [29].

C. Vernier Control

Figure 6 shows the AC-DC converter (see, [27]) control of the vernier. The AC-DC converter is responsible for maintaining the DC-link voltage V_{dcver} through controller gains K_{pDC} and K_{iDC} in addition to the volt-VAr control of the commutating bus through controller gains K_{pQ}, K_{iQ}, K_{pV}, and K_{iV}. Traditional vector control with inner current control loops are employed. The volt-VAr control forms a cascaded structure with a slow reactive power tracking loop generating an AC voltage reference E_{ac}^* for a faster voltage regulation loop.

IV. Allowable Generation Loss or Load Increase

As discussed earlier, the Hybrid-HVDC link can participate in the frequency regulation market to operate under a condition that allows circulating power flow. However, it is important to predetermine the maximum allowable loss of generation or load increase in the inverter-side grid that can be tolerated while providing secondary frequency regulation. This will help quantify the degree of support and facilitate participation in market. There are three constraints that need to be considered – underfrequency load shedding (UFLS) constraint in the rectifier-end, the same at the inverter-side grid, and overall stability constraint. The factors influencing these constraints are as follows:

- Maximum available power ΔP_{head} from the deloaded condition of WF.
- Maximum margins of Vernier voltages (ΔV_{verR}^{max}, ΔV_{verI}^{max}), which depend on the initial values of V_{verR} and V_{verI}.
- Governor droop coefficients K_{gr} and K_{gi} of the synchronous machines G_r and G_i, respectively.
- Droop coefficient K_{wf} for frequency regulation from the WF.

It is assumed that loss of generation can be equivalently represented by increase in load. With any change in load at the inverter end, the power balance equation can be expressed as:

$$\Delta P_{Li} - \Delta P_{di} - K_{gi}\Delta f_i = 0 \tag{5}$$

where, ΔP_{Li}: change in load on the inverter end; ΔP_{di}: change in inverter power; Δf_i: change in frequency of inverter-side AC grid.

For successful AGC action, change in the inverter-end frequency is zero under steady-state, i.e., $\Delta f_i = 0$, which implies that the change in load is compensated by the power transferred through HVDC. Therefore,

$$\Delta P_{Li} = \Delta P_{di} = \Delta P_{cccI} + \Delta P_{verI} \tag{6}$$

where, $\Delta P_{cccI}, \Delta P_{verI}$: change in inverter-side CCC power and Vernier power, respectively.

Assuming that the AC-side voltage of the CCC inverter is constant and the DC current (I_d) is regulated to I_d^0 by the rectifier coordinating control shown in Fig. 5, a constant margin angle γ_i implies CCC DC voltage will remain unchanged. Therefore, CCC power will not change (i.e. $\Delta P_{cccI} = 0$). Hence, equation (6) can be written as:

$$\Delta P_{Li} = \Delta P_{verI} = I_d^0 \Delta V_{verI} \tag{7}$$

where, ΔV_{verI}: change in inverter-side Vernier voltage; I_d^0: regulated DC current by rectifier-side (i.e., $I_d = I_d^0$).

This change in power has to come from the rectifier end. Assuming constant rectifier-side AC voltage, a constant firing angle operation with constant DC current will lead to constant DC voltage of the CCC rectifier, which implies $\Delta P_{cccR} = 0$. This lead to:

$$\Delta P_{Li} = \Delta P_{verR} = I_d^0 \Delta V_{verR} \tag{8}$$

This ΔP_{verR} is shared by G_r and the WF shown in Fig. 2. The increase in load can be expressed as:

$$\Delta P_{Li} = \Delta f_r (K_{gr} + K_{wf}) \tag{9}$$

It is assumed that rectifier AC system operates with rated frequency f_s under nominal condition. Therefore, $\Delta f_r = f_s - f_r$.

From equations (7) and (8), it is clear that the change in Vernier voltages at the rectifier side and inverter side are equal. As a result, for the increase in load, the trajectories followed by the Vernier voltages in $V_{verR} - V_{verI}$ plane will be with a slope of $45°$. Figure 7 shows the family of curves representing the trajectories of Vernier voltages to respond to the increase

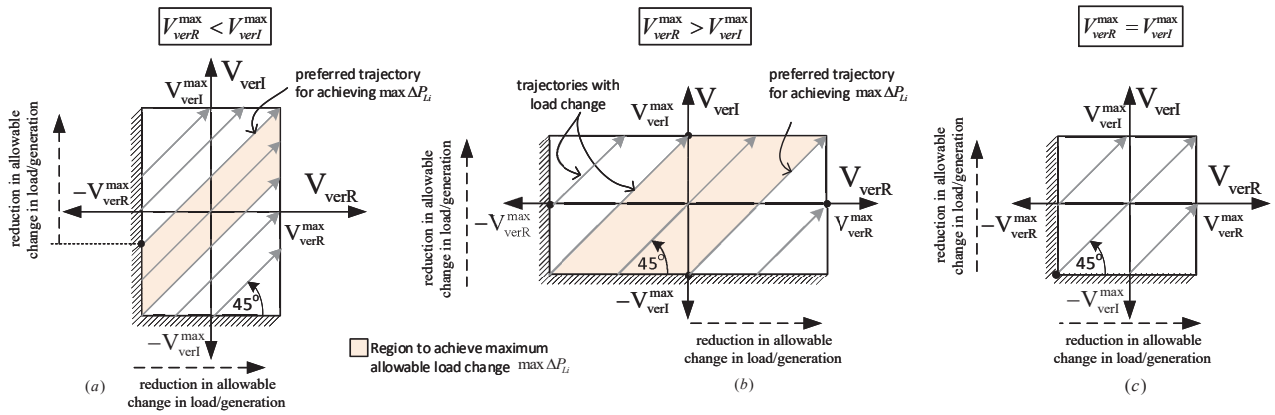

Fig. 7. Vernier voltage trajectories to attain allowable increase in load at the inverter when (a) $V_{verR}^{max} < V_{verI}^{max}$, (b) $V_{verR}^{max} > V_{verI}^{max}$, (c) $V_{verR}^{max} = V_{verI}^{max}$

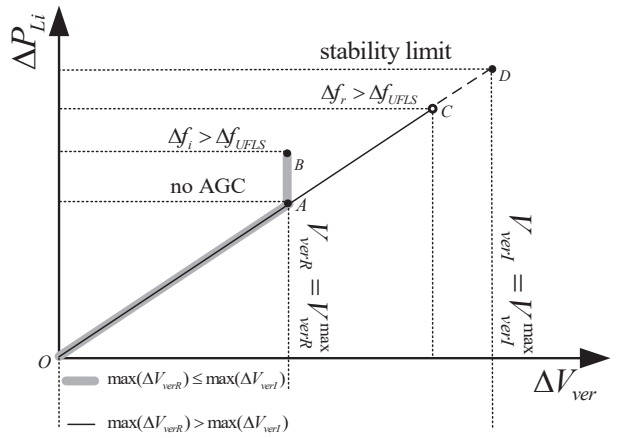

Fig. 8. Characteristics of change in load at the inverter end vs Vernier voltage change to achieve AGC action from inverter control while keeping the system stable.

in load at the inverter end. In this context, three scenarios can be considered: $V_{verR}^{max} < V_{verI}^{max}$, $V_{verR}^{max} > V_{verI}^{max}$, and $V_{verR}^{max} = V_{verI}^{max}$. In the first two cases the operating region in the $V_{verR} - V_{verI}$ plane will be rectangles and in the third case it will be a square, which are shown in Figs 7(a), (b), and (c), respectively. The highlighted regions in Figs 7(a) and (b) permit maximum change in V_{ver}, which in turn can handle maximum load change. For the case in Fig. 7(c) it reduces to a line depicting the diagonal of the square. The operators will prefer to have the nominal operating point (V_{verR}^0, V_{verI}^0) on the shaded boundary of the $V_{verR} - V_{verI}$ plane. As marked in Fig. 7, trajectories outside the highlighted region will lead to a reduction in allowable change in load/generation.

The question however is – *which one is the most preferred trajectory among the others to achieve the maximum load change?* For $V_{verR}^{max} = V_{verI}^{max}$, there is only one trajectory – so we don't have any choice. For the two other cases, the most preferred trajectories are marked in Fig. 7(a) and (b). The basis of the choice is to minimize the length of the trajectory in quadrant III and maximize it in quadrant I in order to minimize losses due to circulating power.

The amount of secondary frequency support can be quantified by the maximum allowable load increase for which the inverter-side frequency can be brought back to its rated value. This can be expressed as:

$$max(\Delta P_{Li}) = \min[(V_{verR}^{\max} - V_{verR}^0)I_d^0, (V_{verI}^{\max} - V_{verI}^0)I_d^0, K_{gr}\Delta f_{UFLS} + \Delta P_{head}] \quad (10)$$

where, $\Delta f_{UFLS} = f_s - f_{UFLS}$, $\Delta P_{head} = (1 - K_d)K_{opt}\omega_r^3$.

As observed from equation (10), the maximum allowable load increase depends upon the initial operating condition determined by V_{verR}^0, V_{verI}^0, I_d^0, and maximum voltage margin $\max(\Delta V_{ver}) = (V_{ver}^{\max} - V_{ver}^0)$. Three cases are considered, which determine the limits on increase in load.

Case I: $\max(\Delta V_{verR}) \le \max(\Delta V_{verI})$: It is clear from equations (7) and (8) that the increase in load depends on the limits of both the Vernier voltages. In this case, V_{verR} hits its maximum limit first. The increase in inverter side reference voltage demands higher voltage from rectifier in order to keep constant current control on the rectifier (Fig. 5); since V_{verR} is saturated, V_{cccR} needs to increase. In this situation, control over firing angle α_r is lost due to the limit hitting of V_{verR}. Since CCC is already operating at minimum α_r; V_{cccR} cannot increase any further. As a result, the rectifier loses control over the current (as V_{verR} and α_r^* hits limit, see, Fig 5) and the inverter CC loop (Fig. 4) becomes active. The control over the inverter-side grid frequency is lost (which depends on the modulation of V_{di}^*), see Fig. 4. Therefore, the support coming from the HVDC rectifier is no longer available and the frequency of the inverter-side grid deviates from the rated value. Following the loss of AGC action, the value of P_{Li} can increase further till $\Delta f_i > \Delta f_{UFLS}$.

Case II: $\max(\Delta V_{verR}) > \max(\Delta V_{verI})$: In this case, due to the increase in the margin of V_{verR}, the load can be further increased unless V_{verI} hits the limit. V_{verI} limit determines the stability of the system as V_{verI} is responsible for operating the system under minimum margin angle γ_i. When V_{verI} hits limit, the increase in the voltage demand has to come from CCC, for that γ_i needs to reduce further. This is not possible as the system is already operating with minimum γ_i. As a consequence, the system becomes unstable.

Case III: $\Delta f_r > \Delta f_{UFLS}$: Apart from the V_{ver} limits, the limit on the rectifier-side frequency deviation has to be imposed. When $\Delta P_{Li} > (K_{gr}\Delta f_{UFLS} + \Delta P_{head})$, it is possible that $\Delta f_r > \Delta f_{UFLS}$ condition is reached even before the limits of V_{ver} are hit. If $K_{wf} >> K_{gr}$, then the WF is dominant in regulating the frequency on the rectifier end. In this condition, if the increase in load exceeds ΔP_{head}; f_r may fall into the UFLS range.

Figure 8 shows the constraints described above for different cases. The linear relation between ΔP_{Li} and ΔV_{ver} is evident from equations (7) and (8). The gray trace (OAB) in Fig. 8 represents Case I. At point A, V_{verR} hits its maximum limit, hence the rectifier loses control over the current and the inverter CC loop becomes active. The control over the inverter-side grid frequency is lost, thus, HVDC will not support AGC action. From point A to B, the increase in load is compensated only by the inverter-side grid and depending on the load increase, frequency may fall under the UFLS range. Point B, shows the maximum load increase beyond which $\Delta f_i > \Delta f_{UFLS}$. The characteristic for Case II is shown with black trace (OAD) in Fig. 8. From point O to A, it follows the same curve as in Case I. Since in this case V_{verR} does not hit the limit, HVDC will keep supporting AGC action on the inverter end as long as V_{verI} hits the limit. Case III characteristic coincides with Case II, but the point of operation till which the frequency support can be given is primarily determined by ΔP_{head} of the WF (assuming $K_{wf} >> K_{gr}$). If WF frequency support is limited, the rectifier side frequency can fall below UFLS range. This operating condition is shown in Fig. 8 with point C. This point can vary depending on the frequency support from the WF and the frequency-droop characteristics of G_r. To evaluate the effectiveness of the proposed scheme for AGC, time-domain simulations are performed, which is presented next.

V. Case Study

The test system in Fig. 2 is considered in the case study, which is represented using a fundamental frequency phasor model. The synchronous machines G_r and G_i are represented by sixth-order subtransient models; the Hybrid HVDC model follows reference [27] where the SCR on both side of HVDC is 2.5; the DFIG-based WF model takes into account a two-mass wind turbine, averaged models of converters, and control loops including inner current control loops in $d-q$ frame. Some of the test system data are mentioned in Appendix.

A. Time-domain Response

Under the nominal condition, V_{verR} is -11 kV and V_{verI} is -21.6 kV. The dynamic performance of the test system is investigated with step increase in P_{Li} by 28 MW at the inverter end under the following three cases:

Case 1: No frequency support from HVDC to the AC grid at inverter end. WF is in MPPT at the rectifier end.

Case 2: Secondary frequency support through inverter control to the AC grid on the receiving end. WF is in MPPT at the rectifier end.

Case 3: Secondary frequency support from inverter control to the AC grid on the receiving end and primary frequency support through deloaded WF control to the AC grid of rectifier-end by keeping the operating conditions same as in *Case 2*.

A 28 MW increase in load is chosen as it results in the inverter-side frequency reach an assumed UFLS threshold of 59.5 Hz.

Figure 9 shows the system response following a step increase in the load by 28 MW at the inverter end. In *Case 1*, HVDC does not participate in AC grid disturbance due to the constant DC voltage control of the inverter. Therefore, there is no change in the HVDC power, as load change is compensated through the synchronous generator power, P_{gi}, see Fig. 9(c). As a result, the frequency f_i falls in the range of UFLS as shown in Fig. 9(a). In *Case 2*, with the proposed supplementary control in HVDC inverter, HVDC extracts the power demanded by load from the rectifier side and thus provides AGC action on the inverter side grid. In this case, the power from the generator G_i (Fig. 2) settles to pre-disturbence value while the HVDC power has increased to provide the additional power. In *Case 3*, power is extracted from the deloaded condition of WF at the rectifier end. This does not change the dynamics of the inverter end, see Figs 9(a), (c).

The rectifier-end system response with increase in the inverter-side load is shown in Figs 9 (b) and (d). Since in *Case 1* HVDC is not participating in frequency support, no change appears on the rectifier-side frequency or power of the grid. On the other hand in *Case 2*, the rectifier side DC power will increase, which can come from either WF or synchronous generator, or both. Since in *Case 2* WF is operating in MPPT - its power output remains constant. The power demanded is evacuated from the rectifier side synchronous generator G_r. Assuming droop coefficients of the same order for G_r and G_i, the rectifier-side frequency will settle at a value close to the inverter grid frequency in the *Case 1* i.e., $59.5Hz$, shown in

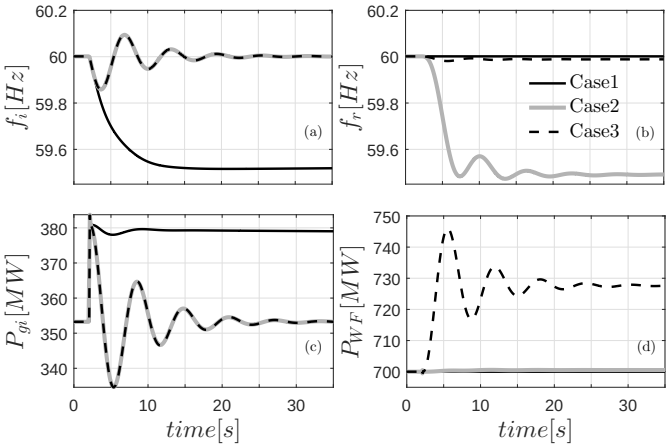

Fig. 9. Dynamic response of the system at inverter and rectifier end with step increase in load on inverter side by 28 MW.

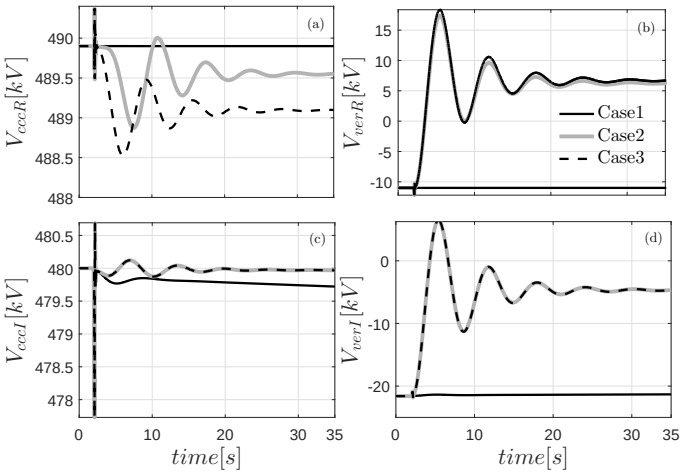

Fig. 10. Change in DC-voltages of CCC and Vernier at both ends of HVDC with the step increase in load by 28 MW in inverter side.

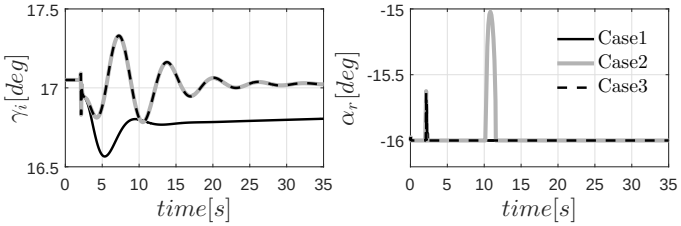

Fig. 11. Change in margin angle γ_i and firing angle α_r with the step increase in load by 28 MW on inverter end.

Fig. 9 (b). In order to prevent rectifier-side grid frequency from falling in the range of UFLS, *Case 3* is considered, in which the WF is operating under deloaded condition and provides the primary frequency support to the AC grid at the rectifier end.

It is essential to understand the distribution of power and voltage among the CCCs and Verniers at the rectifier and inverter ends. Figure 10 shows the change in DC voltages across CCCs and Verniers. In *Case 2*, the Vernier DC voltages V_{verR} and V_{verI} increases due to modulation in reference voltage by $\Delta V_{verI} \approx \Delta V_{verR} \approx 16kV$, while CCC voltages V_{cccR} and V_{cccI} remain unchanged for all practical purposes due to constant firing angle and margin angle controls shown

in Fig. 11. Note that the reason behind the blip in α_r is due to the oscillation in the system. The oscillation generates nonzero $\Delta\alpha_r$, which is being added to $\alpha^*_{r_{min}}$ (see Fig. 5).

Among all the cases, $Case3$ is the most appropriate way to improve frequencies of AC grids on both ends of the Hybrid-HVDC system with its coordinating control scheme. From now on, we will only consider *Case 3*.

B. Constraints on Load Change

From the time-domain study it is clear that the proposed scheme has the potential to provide AGC support to the inverter-side grid. Due to the complexity of the study system it is essential to find the theoretical limits on the change in load in order get AGC support through the HVDC control. Considering the constant DC current, the limit can be calculated through the maximum available voltage margin of the Vernier, $max(\Delta V_{ver})$ $(= V^{max}_{ver} - V^0_{ver})$ at both the ends. For the 75% of rated power flow through the HVDC, the nominal values of Vernier voltages V^0_{verR} and V^0_{verI} are -11 kV and -21.6 kV, respectively (in quadrant III, see Fig. 3(b)). For the constant DC current of 1.64 kA, and same maximum limit of 40 kV for both the Vernier voltages, the maximum available Vernier voltage margins ($max(\Delta V_{verR})$ and $max(\Delta V_{verI})$) are 51 kV and 61.6 kV respectively. Therefore, the maximum allowable increase in load (see, equation (7) and (8)) is 83.64 MW for Case I. For Case II we remove the upper limit on V_{verR}, which leads to a maximum allowable load increase of 101.02 MW.

The $\Delta P_{Li} - V_{verR}$ and $\Delta P_{Li} - V_{verI}$ characteristics are plotted in Fig. 15. We perform multiple nonlinear time-domain simulation for Case I and Case II with different ΔP_{Li} values and plot the characteristics with dashed gray curves. The curves deviate from theoretical prediction at around 50 MW of ΔP_{Li}. This happens due to large oscillations in V_{verR} and V_{verI} shown in Figs 10(b), (d) leading to saturation limit hitting in controllers – see Figs 4 and 5. As shown in Fig. 15, the maximum allowable ΔP_{Li} is 50 MW and 70 MW for Case I and II, respectively – much less compared to theoretical limits. To improve the utilization of Vernier capacity, the existing controller parameters needs to be re-tuned and/or a supplementary compensator needs to be designed to better damp the oscillatory behavior. This is described next.

C. Improvement in Damping

The above-mentioned time-domain simulations were performed using nonlinear state-space averaged phasor model of the test system in the form of the following differential and algebraic equations (DAEs):

$$\dot{x} = f\left(x, u, z\right); 0 = g\left(x, u, z\right) \tag{11}$$

where, x, u, and z are the state, input, and algebraic variables, respectively. The details of the equations are mentioned in references [27], [29]. For *Case 3*, this nonlinear averaged model is linearized around the operating point and expressed in the state-space form as:

$$\Delta\dot{x} = A\Delta x + B\Delta u \tag{12}$$

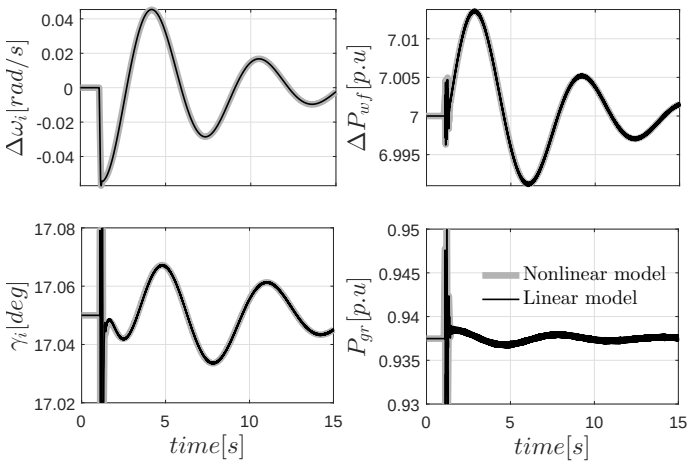

Fig. 12. Validation of the response of linearized state-space model against nonlinear averaged model following pulse change in load at the inverter end.

where, Δx and A are the state vector and the state matrix, respectively. For linearization, the numerical perturbation technique is used through 'linmod' command of Lapack routine in MATLAB 2016a. This linearized model is validated against the nonlinear averaged model.

Figure 12 shows the accuracy of the linearized state-space model against the nonlinear averaged model with the dynamic response of the system following a pulse change in load at the inverter side. Linearization reveals three dominant modes of frequencies $0.119Hz$, $0.138Hz$, and $0.162Hz$. The $0.162Hz$ mode (i.e., $-0.16 \pm j1.017$) has the least damping compared to the other two modes. To improve the damping of this mode, eigenvalue sensitivities with respect to different controller parameters are calculated, which is explained next.

1) Eigenvalue sensitivity: Eigenvalue sensitivity analysis was performed to examine the effect of variation of controller parameters on the unstable modes. The 1^{st}-order eigenvalue sensitivity is given as [30]:

$$\frac{\partial\lambda_i}{\partial\Gamma} = \frac{\psi_i \frac{\partial A}{\partial\Gamma}\phi_i}{\psi_i\phi_i} \tag{13}$$

where, Γ is a system parameter. The sensitivity was approximated by $\frac{\psi_i \frac{\Delta A}{\Delta\Gamma}\phi_i}{\psi_i\phi_i}$, where ΔA denotes the change in the state-matrix corresponding to a small change in parameter Γ, and ψ_i and ϕ_i are the left and the right eigenvectors of eigenvalue $\lambda_i = \sigma_i + j\omega_{di}$. The eigenvalue-sensitivity is computed by reducing the controller gains. Therefore, a positive $\frac{\partial\sigma_i}{\partial\Gamma}$ indicates the real part of the eigenvalue is moving towards left and a positive $\frac{\partial\omega_{di}}{\partial\Gamma}$ indicates a reduction of the value ω_{di}.

Table I shows the eigenvalue sensitivities with respect to the Vernier controller gains, WF's frequency droop coefficient and inverter secondary frequency controller gain. Among all the controllers, the poorly damped mode of $0.162Hz$ has the highest sensitivity with respect to the inverter-side Vernier reactive power controller gain K_{iQ-I} (highlighted in Table I). Therefore, Vernier Q-controller parameter (see Fig. 6) K_{iQ-I} is tuned using root-locus method while utilizing the eigenvalue sensitivity information. Figure 13 shows the eigenvalue movement with increase in K_{iQ-I} value to 10

TABLE I
EIGENVALUE SENSITIVITY ANALYSIS FOR WEAK SYSTEM: SCR =2.5, NOMINAL VALUES $K_{pDC} = 0.012$, $K_{iDC} = 9.0$, $K_{pQ} = 0.01$, $K_{iQ} = 0.10$, $K_{pV} = 0.02$, $K_{iV} = 2.37$. PARAMETERS WERE REDUCED

Mode $\lambda_i = \sigma_i \pm j\omega_d$	K_{pQ-R}	K_{iQ-R}	K_{pQ-I}	K_{iQ-I}	K_{pDC-R}	K_{iDC-R}	K_{pDC-I}	K_{iDC-I}	K_{fi}	K_{wf}
$-0.16 \pm j1.017$	0.003	0.0139	0.267	-0.637	-2.1×10^{-09}	-2.3×10^{-09}	1.4×10^{-06}	-1.2×10^{-07}	0.0156	-4.22×10^{-06}

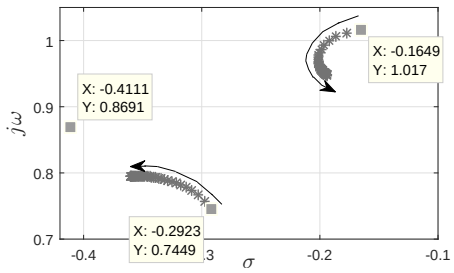

Fig. 13. Eigenvalue movement with increase in K_{iQ-I} value to 10 times of the nominal value.

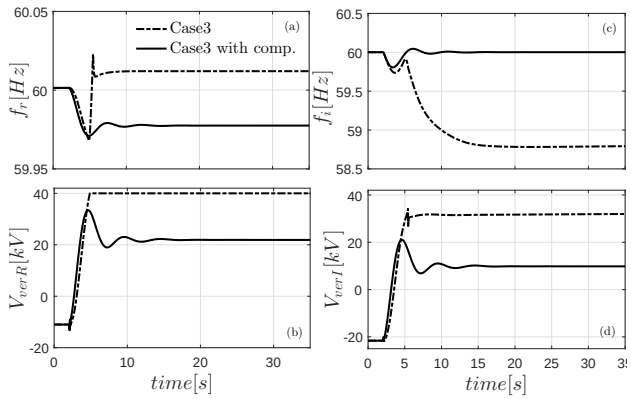

Fig. 14. Effect of compensator design on Vernier voltage and AGC action with increase in load by 52 MW.

times the nominal value. The mode $-0.16 \pm j1.017$ moves towards left and then turns back towards right. This renders the tuning of Q-controller challenging in order to improve its damping. The alternative way is to design a supplementary damping controller, which is explained next.

2) Design of damping controller: The damping controller consists of a simple lead-lag compensator with a gain element, which is designed using pole placement technique [30] - see Appendix for a brief description. The structure of the controller is shown in Fig. 4 and the parameters in the Appendix. The new pole location is chosen to satisfy the settling time to be 10 s. The imaginary part is chosen to be slightly higher than that of the 0.162-Hz mode. Table II shows the improvement in the damping and settling time of the poorly-damped mode of 0.162 Hz. The controller does not affect the two other modes negatively.

TABLE II
IMPROVEMENT IN THE CRITICAL MODES AFTER INCLUDING COMPENSATOR IN CASE3

Case3			*Case3* with comp.		
$\xi, \%$	f, Hz	Ts, sec	$\xi, \%$	f, Hz	Ts, sec
36.5	0.119	13.38	43.0	0.112	11.95
42.8	0.138	9.73	42.7	0.138	9.73
16.0	0.162	24.25	28.2	0.199	10.88

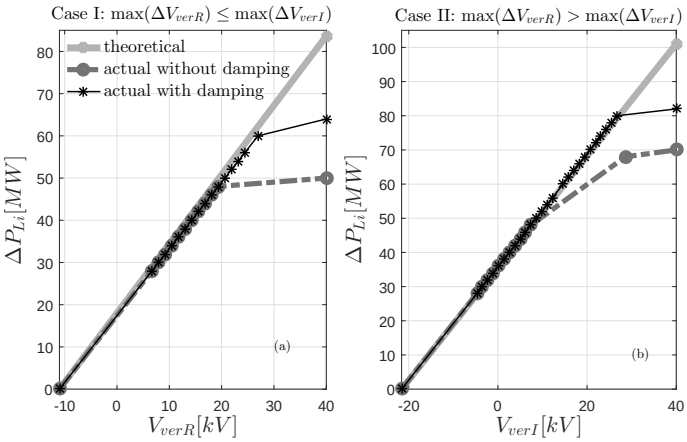

Fig. 15. Theoretical and actual $\Delta P_{Li} - V_{ver}$ characteristics with and without damping controller.

D. Improvement in Vernier utilization

As shown in Fig. 14, the rectifier-side Vernier voltage V_{verR} hits the limit following an increase in P_{Li} by 52 MW when no compensator is used. As a result, the AGC action is lost. With the designed compensator, the Vernier voltage settles to a lower value. Thus the full range of Vernier voltage can be utilized to accommodate larger change in the load while providing AGC action at the inverter end.

Figure 15 shows the $\Delta P_{Li} - V_{ver}$ characteristics obtained from nonlinear simulations when the compensator is enabled. It can be seen that the range of allowable ΔP_{Li} has increased from 50 MW to 64 MW in Case I (see, Fig 15(a)), and from 70 MW to 82 MW in Case II (see, Fig 15(b)).

VI. CONCLUSION

Some new findings and ideas relating Hybrid High Voltage DC (HVDC) system comprising a Capacitor Commutated Converter connected in series with a 2-stage Voltage Source Converter called 'Vernier' were presented. It was shown that the flexible voltage polarity of the Vernier leads to circulating power, which gives extra degrees of freedom to the controls. These were used to provide secondary frequency support in the inverter-side grid while benefiting from constant firing angle and extinction angle operation. The frequency support contribution through the Hybrid-HVDC link was analytically quantified in terms of the maximum allowable load increase in the inverter end. This contribution and constraints relating underfrequency load shedding and system stability were validated using nonlinear time-domain simulations. Finally, it was shown that a damping controller designed to improve the dynamic behavior of the system can increase utilization of the Vernier capacity.

APPENDIX

Test system parameters

Variables	*Rating*	*Nom.Cond.*
Power (MW)	1000	785
Inv. DC voltage (kV)	500	478.9
DC current (kA)	2	1.64
Inv. Vernier voltage (kV)	± 40	-21.6
Rec. Vernier voltage (kV)	± 40	-11.0
AC grid voltage (kV)	345	345

Transformer rating: $345/182kV$; $557MVA$,
Transformer leakage inductance, $L_c = 0.12\ pu$
DC Line parameters:
$R_L = 12.5\ \Omega$, $L_{dc} = 1.4515H$, $C_{dc} = 13.6\mu F$
Series capacitor of CCCs: $C_r = C_i = 112\mu F$
Line impedance:
$Z_1 = Z_2 = 2.18 + j47.59\ \Omega$,
$Z_3 = Z_4 = 0.012 + j0.09\ \Omega$
Droop coefficient (in $pu - MW.s$) on 100MWA base:
K_{gr} = 166.7, K_{gi} = 200, K_{wf} = 31.4
Nominal power output (in MW):
P_{gi} = 352.8, P_{gr} = 87.6, P_{wf} = 700
Inverter voltage controller gains:
$K'_{pi} = 187.53$; $K'_{ii} = 6250\ s^{-1}$; $K_{verI} = 1$; $K_{\gamma i} = 1\ kV/rad.s$
Supplementary frequency controller gains:
$K_{fi} = 15\ kV/rad$; $K_c = 15.19$; $T_1 = 0.5067$; $T_2 = 1.326$;
Rectifier current controller gains:
$K_{ir} = 187.53\ kV/kA.s$; $K'_{pr} = 6250\ \Omega$; $K_{verR} = 1$; $K_{\alpha r} = 1\ kV/rad.s$
Damping controller parameters:
$K_c = 15.19$; $T_1 = 0.5067$; $T_2 = 1.326$

Design of lead lag compensator

The compensator has a following lead/lag structure:

$$H(s) = K_c \frac{1 + T_1 s}{1 + T_2 s} \tag{14}$$

Considering $G(s)$ to be the transfer functions of the plant, the closed-loop transfer function of the compensated plant is derived as:

$$G_c(s) = \frac{G(s)}{1 - G(s)H(s)} \tag{15}$$

The eigenvalue $-0.16 \pm j1.017$ corresponding to 0.162Hz mode is shifted to a new value location in the s-plane denoted by λ_0. Since λ_0 satisfy the characteristic equation of the closed-loop system (see, (15)),

$$H(\lambda_0) = \frac{1}{G(\lambda_0)} \tag{16}$$

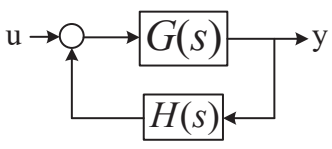

Fig. 16. Transfer function of the plant and compensator in feedback

This can be expressed as magnitude and phase as follows:

$$|H(\lambda_0)| = \frac{1}{|G(\lambda_0)|}; \qquad \arg(H(\lambda_0)) = -\arg(G(\lambda_0)) \tag{17}$$

The magnitude and phase of the compensator at λ_0 (i.e., $H(\lambda_0)$) and thus the value of time constants T_1 and T_2 from equation (14) can be calculated from the magnitude and phase of the the plant at λ_0, i.e., $G(\lambda_0)$.

REFERENCES

[1] "IEEE Standard Definitions of Terms for Automatic Generation Control on Electric Power Systems," *IEEE Transactions on Power Apparatus and Systems*, vol. PAS-89, no. 6, pp. 1356–1364, July 1970.
[2] J. Chand, "Auxiliary power controls on the Nelson River HVDC scheme," *IEEE Transactions on Power Systems*, vol. 7, no. 1, pp. 398–402, Feb 1992.
[3] M. Sampei, H. Magoroka, and M. Hatano, "Operating experience of Hokkaido-Honshu high voltage direct current link," in *Proceedings of 1996 Transmission and Distribution Conference and Exposition*, Sep. 1996, pp. 158–163.
[4] M. Davies, A. Kolz, M. Kuhn, D. Monkhouse, and J. Strauss, "Latest control and protection innovations applied to the basslink HVDC interconnector," in *The 8th IEE International Conference on AC and DC Power Transmission*, March 2006, pp. 30–35.
[5] S. P. Teeuwsen, G. Love, and R. Sherry, "1400 MW New Zealand HVDC upgrade: Introducing power modulation controls and round power mode," in *2013 IEEE Power Energy Society General Meeting*, July 2013, pp. 1–5.
[6] D. Martin, W. Wong, G. Liss, B. Arnlov, T. Jonsson, J. Gleadow, and J. de Silva, "Modulation controls for the New Zealand DC hybrid project," *IEEE Transactions on Power Delivery*, vol. 6, no. 4, pp. 1825–1830, Oct 1991.
[7] C. Guo, C. Zhao, R. Iravani, H. Ding, and X. Wang, "Impact of phase-locked loop on small-signal dynamics of the line commutated converter-based high-voltage direct-current station," *IET Generation, Transmission Distribution*, vol. 11, no. 5, pp. 1311–1318, 2017.
[8] S. Lu, Z. Xu, L. Xiao, W. Jiang, and X. Bie, "Evaluation and Enhancement of Control Strategies for VSC Stations Under Weak Grid Strengths," *IEEE Transactions on Power Systems*, vol. 33, no. 2, pp. 1836–1847, 2018.
[9] J. Fradley, R. Preece, and M. Barnes, "VSC-HVDC for frequency support (a review)," in *13th IET International Conference on AC and DC Power Transmission (ACDC 2017)*, Feb 2017, pp. 1–6.
[10] C. Du, E. Agneholm, and G. Olsson, "Comparison of Different Frequency Controllers for a VSC-HVDC Supplied System," *IEEE Transactions on Power Delivery*, vol. 23, no. 4, pp. 2224–2232, Oct 2008.
[11] G. Persson, V. F. Lescale, and A. Persson, "HVDC capacitor commutated converters in weak networks," GCC Cigre'. https://library.e.abb.com/public/ad88f26d817df269c12577f8006a6f72/GCC%20Cigre_CCC%20in%20weak%20networks_final.pdf [Accessed: 23 - March - 2018].
[12] J. Graham, D. Menzies, G. Biledt, C. Antonio Ricardo, P. Wo Wei, and A. Wey, "Electrical system considerations for the Argentina-Brazil 1000 MW interconnection," in *Cigre 2000 Conference, Paris, France*, 2000.
[13] M. Stoltz, M. Bahrman, D. Dickinson, and B. Abrahamsson, "The Rapid City DC Tie," in *2006 IEEE PES Power Systems Conference and Exposition*, Oct 2006, pp. 476–479.
[14] M. Pinto, A. Pagioro, and R. Azevedo, "The Rio Madeira HVDC System - Implementation and Commissioning of Bipole 1 and the Connector to Acre-Rondonia," *Colloquium, HVDC and Power Electronics to Boost Network Performance, Brazil*, Oct 2013.
[15] R. E. Torres-Olguin, M. Molinas, and T. M. Undeland, "A model-based controller in rotating reference frame for Hybrid HVDC," in *2010 IEEE Energy Conversion Congress and Exposition*, Sept 2010, pp. 1578–1584.
[16] R. E. Torres-Olguin, A. Garces, M. Molinas, and T. Undeland, "Integration of Offshore Wind Farm Using a Hybrid HVDC Transmission Composed by the PWM Current-Source Converter and Line-Commutated Converter," *IEEE Transactions on Energy Conversion*, vol. 28, no. 1, pp. 125–134, March 2013.
[17] O. Kotb and V. K. Sood, "A hybrid HVDC transmission system supplying a passive load," in *2010 IEEE Electrical Power Energy Conference*, Aug 2010, pp. 1–5.

[18] P. Manohar, V. Kelamane, D. Kaushik, and W. Ahmed, "Improved controls for LCC-VSC hybrid HVDC system," in *2013 International conference on Circuits, Controls and Communications (CCUBE)*, Dec 2013, pp. 1–5.

[19] Y. Yu, Y. Lu, and Q. Chen, "Internal model startup control for VSC-LCC based hybrid pseudo bipolar HVDC system," in *2017 2nd International Conference on Power and Renewable Energy (ICPRE)*, Sept 2017, pp. 15–19.

[20] C. Hahn, A. Geub, and M. Luther, "Modeling and control design of hybrid - LCC and VSC based - HVDC systems," in *2016 IEEE/PES Transmission and Distribution Conference and Exposition (T D)*, May 2016, pp. 1–6.

[21] Y. Wang and B. Zhang, "A novel hybrid directional comparison pilot protection scheme for the LCC-VSC hybrid HVDC transmission lines," in *13th International Conference on Development in Power System Protection 2016 (DPSP)*, March 2016, pp. 1–6.

[22] W. Liu, C. Zhao, and C. Guo, "The control strategy for Hybrid HVDC using voltage margin control and voltage dependent current order limiter control," in *2nd IET Renewable Power Generation Conference (RPG 2013)*, Sept 2013, pp. 1–4.

[23] Y. Lin, Z. Xu, L. Xiao, Z. Zhang, and H. Xiao, "Analysis of coupling effect on LCC-MCC hybrid HVDC from parallel AC lines in close proximity," in *2015 IEEE Power Energy Society General Meeting*, July 2015, pp. 1–5.

[24] R. Zeng, L. Xu, L. Yao, S. J. Finney, and Y. Wang, "Hybrid HVDC for Integrating Wind Farms With Special Consideration on Commutation Failure," *IEEE Transactions on Power Delivery*, vol. 31, no. 2, pp. 789–797, April 2016.

[25] G. Lee, D. Kwon, S. Moon, and C. Kim, "Control strategy for hybrid high-voltage DC systems connecting voltage-weak grids," in *2017 IEEE Power Energy Society General Meeting*, July 2017, pp. 1–5.

[26] N. R. Chaudhuri, R. Gupta, and E. Larsen, "Hybrid high voltage direct current converter system and method of operating the same," U.S. Patent 9 602 021 B2, (assignee: General Electric Company), March 21, 2017.

[27] J. Kaur and N. R. Chaudhuri, "A Coordinating Control for Hybrid HVDC Systems in Weak Grid," *IEEE Transactions on Industrial Electronics*, pp. 1–1, 2019.

[28] M. F. M. Arani and Y. A. I. Mohamed, "Analysis and impacts of implementing droop control in DFIG-based wind turbines on microgrid/weak-grid stability," *IEEE Transactions on Power Systems*, vol. 30, no. 1, pp. 385–396, Jan 2015.

[29] A. Yogarathinam, J. Kaur, and N. R. Chaudhuri, "Impact of Inertia and Effective Short Circuit Ratio on Control of Frequency in Weak Grids Interfacing LCC-HVDC and DFIG-Based Wind Farms," *IEEE Transactions on Power Delivery*, vol. 32, no. 4, pp. 2040–2051, Aug 2017.

[30] P. Kundur, *Power system stability and control*, ser. The EPRI power system engineering series. New York; London: McGraw-Hill, 1994.

Jagdeep Kaur (S'15) received her M.Tech degree in Power Electronics, Electrical Machines & Drives from Indian Institute of Technology (IIT) Delhi, India in 2013 and her Ph.D. degree from the Pennsylvania State University, USA in 2019. Her research interests include power electronics, electrical machine drives, HVDC, renewable energy, smart grids, model reduction, and application of power electronics in power systems.

Nilanjan Ray Chaudhuri (S'08-M'09-SM'16) received his Ph.D. degree from Imperial College London, London, UK in 2011 in Power Systems. From 2005-2007, he worked in General Electric (GE) John F. Welch Technology Center. He came back to GE and worked in GE Global Research Center, NY, USA as a Lead Engineer during 2011-2014. Presently, he is an Assistant Professor with the School of Electrical Engineering and Computer Science at Penn State, University Park, PA. He was an Assistant Professor with North Dakota State University, Fargo, ND, USA during 2014-2016. He is a member of the *IEEE* and *IEEE PES*. Dr. Ray Chaudhuri is the lead author of the book *Multi-terminal Direct Current Grids: Modeling, Analysis, and Control* (Wiley/IEEE Press, 2014)). He served as an Associate Editor of the IEEE TRANSACTIONS ON POWER DELIVERY (2013 2019) and IEEE PES LETTERS (2016 - present). Dr. Ray Chaudhuri was the recipient of the National Science Foundation Early Faculty CAREER Award in 2016 and Joel and Ruth Spira Excellence in Teaching Award in 2019.